

## Role of substrate corrugation in helium monolayer solidification

M. E. Pierce and E. Manousakis

*Department of Physics and Center for Materials Research and Technology, Florida State University, Tallahassee, Florida 32306-4350*

(Received 23 November 1999; revised manuscript received 28 February 2000)

We investigate the first layer of helium adsorbed on graphite with path-integral Monte Carlo, examining the role of substrate corrugations on the phase diagram. When no corrugations are present, the equilibrium state of the system is a liquid phase, with solidification occurring only under compression but before layer promotion. We determine the solid-liquid coexistence region and compare our results to recent Green's-function Monte Carlo calculations on the same system. When substrate corrugations are included, we find that the equilibrium phase is the  $\sqrt{3} \times \sqrt{3}$  commensurate solid phase that is well known from experiment. The melting behavior, heat capacity, and single-particle binding energy are determined and compared to experiment. We further find that for densities below the commensurate coverage, the low-temperature phase of the system consists of solid clusters in coexistence with coalesced vacancies. We find no first-layer liquid phase and so no superfluidity in this layer, in contrast to some rather recent suggestions.

### I. INTRODUCTION

Quantum films such as helium adsorbed on a graphite surface are characterized by a rich phase diagram as one varies the number of the deposited helium atoms. As a function of the helium coverage, the helium film grows in atomically thin layers<sup>1-3</sup> and at least seven such layers may be clearly distinguished and studied on a well-prepared substrate.

During the last several years, extensive heat-capacity measurements<sup>4-6</sup> of the first six layers have been performed, and superfluidity in the higher layers has been detected by both torsional oscillator<sup>7,8</sup> and third sound measurements. More specifically, the first layer of helium adsorbed on graphite has been the laboratory for the study of a variety of phenomena. In this layer a  $\sqrt{3} \times \sqrt{3}$  commensurate solid phase forms in which one-third of the available substrate adsorption sites are occupied.<sup>4,6,9,10</sup> For densities above this commensurate density, the monolayer is characterized by a region of domain wall phases and at even higher monolayer densities it forms an incommensurate triangular solid phase.<sup>11-13</sup> The phase diagram below the commensurate density at low temperatures is not well understood and there are two competing scenarios. In one scenario this region corresponds to a solid with clustered vacancies.<sup>14</sup> According to this picture, since the commensurate solid phase is in the same universality class as the three-state Potts model,<sup>15-19</sup> at lower densities the film should consist of a commensurate solid with vacancies. When the temperature is raised, the solid melts continuously. Lowering the temperature causes the vacancies to coalesce, which is a first-order transition. The difference between the temperatures of these two transitions becomes smaller as the density is lowered until they meet at a tricritical point.

The second scenario for the low-density region of the phase diagram of the submonolayer was suggested more recently by Greywall and Busch<sup>5</sup> (GB). GB point out that their measured heat capacity is not linear in density for the entire region below the commensurate density, as it must be for phase coexistence. Thus, they propose that a self-bound liq-

uid phase occurs at about 0.04 atom/Å<sup>2</sup>. This conclusion is supported by two-dimensional (2D) variational calculations.<sup>20</sup> However, direct measurements<sup>7,8,21</sup> detect no superfluidity, possibly because of poor substrate connectivity.

In a previous publication,<sup>22</sup> we have used the path-integral Monte Carlo method and realistic helium-helium and helium-graphite interactions to study the monolayer at or below the commensurate density. We found that the presence of corrugations, which causes the commensurate solid at 1/3 coverage, creates solid commensurate clusters at densities below the commensurate density. We found that it is the melting of these monolayer clusters which gives rise to a specific-heat maximum which was incorrectly interpreted<sup>5</sup> as the onset of monolayer superfluidity. In this paper we examine in detail the role of substrate corrugation on the first-layer phase diagram using the path-integral Monte Carlo method. First, we present results for helium adsorbed on a smooth substrate. The helium-graphite interaction is based on the laterally averaged potential of Carlos and Cole.<sup>23</sup> This layer exhibits liquid and solid phases, and we calculate the phase diagram at low temperatures. These results are compared with recent Green's-function Monte Carlo calculations.<sup>24</sup> The second-layer promotion density is also determined. Next, calculations including substrate corrugations are discussed, and direct comparisons of the melting behavior, specific-heat, and single-particle binding energy that we obtain are made with experiment. Finally, having verified our method by the above comparisons, we examine the low-density, low-temperature phase of the helium monolayer. We determine that for all coverages below the commensurate density, the system consists of solid clusters in phase coexistence with coalesced vacancies. No liquid phase occurs and so there is no possibility for first-layer superfluidity.

### II. SIMULATION METHOD

Our study employs a path-integral Monte Carlo (PIMC) method for simulating Bose systems. Details on the application of this method to bulk helium can be found in the review by Ceperley,<sup>25</sup> and our modifications for the simulation of

adsorbed helium films may be found in a previous publication.<sup>26</sup> We briefly review the procedure now in order to explain the calculations presented in this paper.

PIMC evaluates properties of an  $N$ -body quantum system at the inverse temperature  $\beta$  by sampling the partition function  $Z$ .  $Z$  is expanded as a path integral by inserting  $M$  intermediate configurations,

$$Z = \frac{1}{N!} \sum_P \int \dots \int d^3R_1 \dots d^3R_M d^3R \rho(\mathbf{R}_1, \mathbf{R}_2; \tau) \times \rho(\mathbf{R}_2, \mathbf{R}_3; \tau) \dots \rho(\mathbf{R}_M, P\mathbf{R}_1; \tau), \quad (1)$$

where  $\rho$  is the density matrix,  $\mathbf{R}_i$  is a configuration of  $N$  particles, and  $\tau = \beta/M$ . By taking  $M$  large enough, the density matrices at  $\tau$  can be accurately approximated. The particular PIMC method that we employ ergodically samples both particle positions and particle permutations.

The key element needed in the first-layer simulation is an accurate approximation for the high-temperature density matrices. For bulk helium and helium on a smooth substrate, the starting approximation for the density matrix can be taken with a temperature as low as 40 K. In this paper results for the first layer on a smooth substrate were obtained using the same starting approximation for the density matrix that was used in previous calculations for the second layer.<sup>26</sup>

However, as discussed in our previous publication,<sup>26</sup> a helium-graphite interaction that includes substrate corrugations makes the starting approximation used for smooth substrates impractical, and so we must use a simpler form. For these calculations, we instead use the high-temperature expansion of the density matrix. At sufficiently small values of the inverse temperature, the density matrix is given by the Trotter approximation,

$$\exp(-\tau\hat{H}) \approx \exp(-\tau\hat{T})\exp(-\tau\hat{V}), \quad (2)$$

where  $\hat{H}$ ,  $\hat{T}$ , and  $\hat{V}$  are the Hamiltonian and the kinetic- and potential-energy operators, respectively, and  $\tau$  is the inverse temperature. This allows us to approximate the density matrices at  $\tau$  as

$$\rho(\mathbf{R}, \mathbf{R}'; \tau) \approx \exp[-\pi(\mathbf{R}_i - \mathbf{R}_{i+1})/\lambda_T^2 - \tau[V(\mathbf{R}_i) + V(\mathbf{R}_{i+1})]/2], \quad (3)$$

where  $R$  and  $R'$  are the position vectors for  $N$ -particle configurations, and  $\lambda_T$  is the thermal wavelength. This is sometimes referred to as the semiclassical approximation, and is accurate for sufficiently high starting temperatures. Averaging over the potential-energy terms is referred to as the endpoint approximation. The potential energy term  $V(\mathbf{R}_i)$  is the sum of all helium-helium and helium-graphite interactions. The exponent of Eq. (3) is the first term in an expansion in powers of  $\tau$ .<sup>27</sup>

In the semiclassical calculations, we have used 200 K as the starting temperature, meaning that 200 inverse-temperature slices are required to reach 1 K. We have verified that this temperature is sufficiently high for the approximation to be accurate by comparing the energy calculated at 4 K using 200 and 320 K as the starting temperatures. The energy values obtained agreed within error bars. We have also adopted a three-level bisection,  $l=3$ , for sampling the

positions. We verified that this level gave a lower energy at 4 K than calculations using  $l=2$  and  $l=4$ . The acceptance rate using  $l=3$  is approximately 40%. We have further verified that the density matrix is well approximated at 200 K by Eq. (3) by including the next term in the series expansion in powers of  $\tau$ . Energy values calculated with this starting approximation agreed within error bars with those that used Eq. (3).

We did find that higher-order terms in  $\tau$  must be included in the energy estimator. The values we report in Sec. IV are obtained using

$$\langle E \rangle = \frac{3N}{2\tau} + \langle T \rangle + \langle V \rangle + \tau^2 \hbar^2 / (8m) \langle (\nabla V)^2 \rangle \quad (4)$$

for the energy expectation value, where  $N$  is the number of particles,  $\langle T \rangle$  and  $\langle V \rangle$  are the kinetic- and potential-energy expectation values, and  $m$  is the mass of the helium atom. Note that in PIMC the effective action, defined as the natural logarithm of the density matrix, not the energy estimator, is used to choose between configurations in the Monte Carlo procedure.

Once the machinery for the Monte Carlo method is in place, helium-helium and helium-substrate potentials are required for input. We use the Aziz<sup>28</sup> potential for the helium-helium interaction. For the helium-graphite interaction, we have adopted the anisotropic Lennard-Jones potential proposed by Carlos and Cole.<sup>23</sup> This potential can be expressed as a Fourier series in the reciprocal-lattice vectors  $\mathbf{G}$  of the graphite substrate. In cylindrical coordinates  $(\rho, z)$  the expansion is

$$V(\mathbf{r}) = V_0(z) + \sum_{\mathbf{G}} V_{\mathbf{G}}(z) \exp(i\mathbf{G} \cdot \boldsymbol{\rho}), \quad (5)$$

where  $V_0(z)$  is the laterally averaged potential, and  $V_{\mathbf{G}}(z)$  gives the corrugation strength. The mathematical forms for these terms are given elsewhere,<sup>23</sup> and the series converges rapidly. For the smooth substrate, we use only  $V_0(z)$ . For calculations that included corrugations, we kept the six lowest, equivalent values of  $\mathbf{G}$  in the expansion.

The limitation of our method is thus related to the accuracy of the potentials available to us. It is possible, for instance, that the substrate may substantially mediate the helium-helium interaction.<sup>29</sup> This is the so-called McLachlan interaction.<sup>30</sup> We have performed calculations both with and without this term. Another possible concern is the helium-graphite potential, Eq. (5), which may overestimate the corrugation strength. Lowering the corrugation height will effect the properties of the first layer, with the favored phase becoming liquid instead of solid at sufficiently small corrugations. We have examined this effect by repeating some of the calculations with the corrugation strength set to 50% and to 75% of the value obtained from the Carlos-Cole model. Details of these tests of the limits of our interaction model are given below.

Particle permutations were also included in the calculations and were observed in the film on the smooth substrate at low densities. However, we have found that permutations do not play a role in the first layer on the corrugated substrate. We have allowed for permutations at intermediate densities for temperatures as low as 0.571 K with the level of

the path bisectioning taken as large as 5 (32 beads updated in one move) but never observed any particle exchanges. This has been checked in calculations both with and without the McLachlan interaction.

### III. RESULTS FOR SMOOTH GRAPHITE SURFACE

#### A. Energy calculations

In this section we report simulation results for the first layer obtained by using only the laterally averaged portion  $V_0(z)$  of the helium-graphite potential. We ignore substrate corrugations. This system has recently been studied with the Green's-function Monte Carlo (GFMC) method,<sup>24</sup> so we have the opportunity to verify that the full implementation of our method is in agreement with the results of these complementary calculations. The GFMC calculations employ the same helium-graphite potential as we do, but use an older form of the helium-helium potential.<sup>31</sup> The older form was used since the authors wanted to make direct comparisons with previous work on two-dimensional helium using this potential.<sup>32</sup> The newer potential that we use for the helium-helium interaction is somewhat more attractive (the well depth is about 0.1 K greater), so we expect the energy per particle to be somewhat lower near the equilibrium density. This has been observed in recent zero-temperature calculations for two-dimensional liquid helium that employ the newer potential.<sup>33</sup>

Guided by previous simulations, we expect the helium film to have a self-bound liquid phase and to solidify at high densities, before promotion to the next layer occurs. Calculations at low and intermediate densities are performed using a square simulation cell, while solid phase calculations use a rectangular simulation cell that accommodates the periodic structure of the triangular solid. It is not necessary in PIMC to employ different forms for the density matrix for the liquid and solid phases. Liquid calculations employed 16 particles, while solid phase calculations used 30 particles. Both sets of calculations were performed at 400 mK. Calculations at 500 mK are in agreement with these results, indicating that we have converged to the zero-temperature limit. We verified that there were no finite-size errors in the liquid phase by repeating some of the calculations with 32 particles. The energy values at the two temperatures were in agreement. Finite-size errors were found to be negligible for the solid phase also, since the energy value calculated at 0.0689 atom/ $\text{\AA}^2$  using the rectangular simulation cell (30 particles) agreed with the value calculated using the square simulation cell (16 particles).

These calculations are somewhat different from those we discuss in the other section of this paper. The potential between the active helium atoms and the underlying substrate is featureless in the plane of the substrate, so the size of the simulation cell may be varied continuously. This allows us to keep the number of particles constant for each phase. In contrast, other calculations we have performed (including those with substrate corrugations taken into account) were with a varying number of particles and a constant simulation cell size. The two methods lead to somewhat different forms for the Maxwell construction. In the present case, liquid-solid

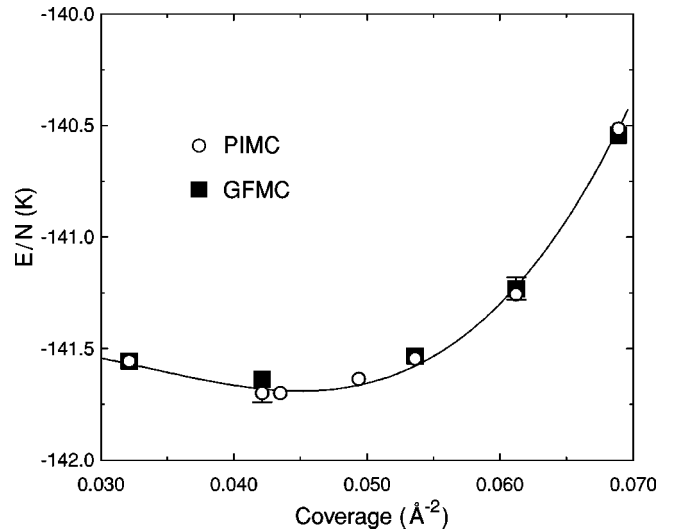


FIG. 1. Energy values for the first-layer liquid. The circles are our results obtained with PIMC. The solid squares are GFMC results (Ref. 24). Error bars smaller than the symbol size are omitted for clarity. The line is a least-squares fit of the polynomial, Eq. (6) to our data.

coexistence will be characterized by a linear region in the dependence of the energy per particle on the atomic area (inverse volume).

Figure 1 displays our results for the energy of the first-layer liquid. Also shown are the results obtained from GFMC. For all points except near equilibrium, the two calculations agree within error bars. Near the energy minimum, there is some disagreement, but even here the computed values differ only by about 0.6%. This is perhaps attributable to the different helium-helium potentials used in the two calculations. Figure 2 shows our results and the GFMC results for the first-layer solid phase. Again, there is excellent agreement between the two methods.

Following the typical procedure, we have determined the equations of state for the liquid and solid phases by fitting our energy values to the polynomials

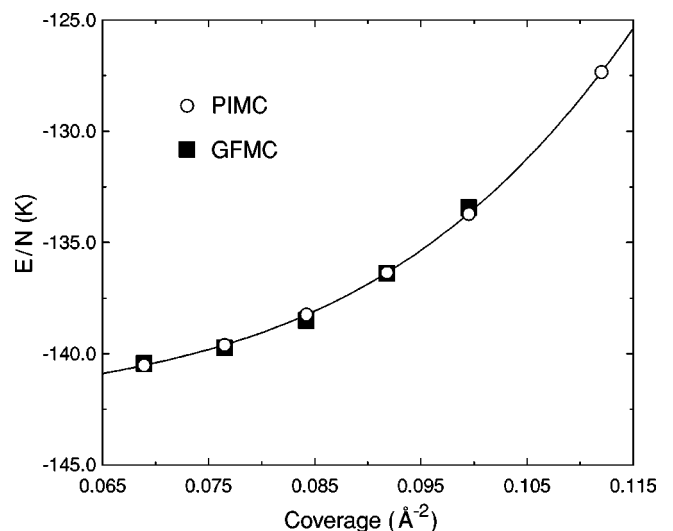


FIG. 2. Energy values for the first-layer triangular solid. The symbols have the same meaning as in Fig. 1. The line is determined from the fit of Eq. (7) to our data.

TABLE I. Fitted parameters for the liquid and solid equations of state. The errors in the last digits of the parameters for the liquid phase are given in parentheses.

Parameter	Liquid	Parameter	Solid
$e_0$ (K)	-141.689(14)	$\alpha$ (K)	-157.46
$\rho_0$ ( $\text{\AA}^{-2}$ )	0.0450(06)	$\beta$ ( $\text{K}/\text{\AA}^2$ )	-679.83
$B$ (K)	2.42(27)	$\gamma$ ( $\text{K}/\text{\AA}^4$ )	-10504.77
$C$ (K)	3.29(67)	$\delta$ ( $\text{K}/\text{\AA}^6$ )	61032.24
$\chi^2/\nu$	2.57	$\chi^2/\nu$	1.3

$$E/N = e_0 + B \left( \frac{\rho - \rho_0}{\rho_0} \right)^2 + C \left( \frac{\rho - \rho_0}{\rho_0} \right)^3, \quad (6)$$

$$E/N = \alpha + \beta\rho + \gamma\rho^2 + \delta\rho^3 \quad (7)$$

for the liquid and solid phases, respectively. Values for the fitted parameters are given in Table I. Errors for the liquid phase are indicated. The values shown for the solid phase were used in the plot of Fig. 2. The values given for  $\beta$ ,  $\gamma$ , and  $\delta$  are accurate to one significant figure.

For the liquid phase, the parameters  $e_0$  and  $\rho_0$  are the equilibrium energy per particle and the equilibrium coverage. The equilibrium density we obtain,  $0.0450 \text{ atom}/\text{\AA}^2$ , is in reasonable agreement with the GFMC value of  $0.0443$ . Below this density, the system enters gas-liquid coexistence in the thermodynamic limit. In simulation, phase separation will not occur immediately because of the finite cost of creating the phase boundary. The system will instead enter a ‘‘stretched,’’ or negative pressure, state. If one continues to decrease the coverage, however, the phase separated state will eventually become the favored state, and the stretched state will ‘‘snap,’’ forming a droplet plus vacuum. For a simulation with a constant number of particles and variable area, this occurs when the derivative of the spreading pressure,  $P = \rho^2[\partial e(\rho)/\partial \rho]$ , is zero. At the spinodal point, the sound velocity becomes imaginary and the compressibility diverges. From the equation of state, we determine that this occurs at  $0.034 \text{ atom}/\text{\AA}^2$ . For comparison, the spinodal density has been calculated to be between  $0.031$  and  $0.038 \text{ atom}/\text{\AA}^2$  for two-dimensional helium.<sup>34,33,32</sup>

From the polynomial fits for the two layers, we can estimate the regions of phase coexistence for the two solids by using the Maxwell double tangent construction. See Fig. 3. Since we have a constant number of particles and a variable density, the Maxwell construction is found from the common tangent of the energy per particle versus atomic area (inverse coverage). We determine the liquid-solid coexistence region to be from  $0.0675$  to  $0.0700 \text{ atom}/\text{\AA}^2$ . This is comparable to the ranges found for both two-dimensional helium<sup>32,35</sup> and the helium film,<sup>24</sup> although the onset of full solidification that we find is at a somewhat lower density. The solidification density determined in this manner is subject to error, since our fitted parameters are not determined with a high degree of precision.

### B. Other properties

As we have seen, in the absence of corrugations, the first layer has liquid-gas, self-bound liquid, liquid-solid, and solid

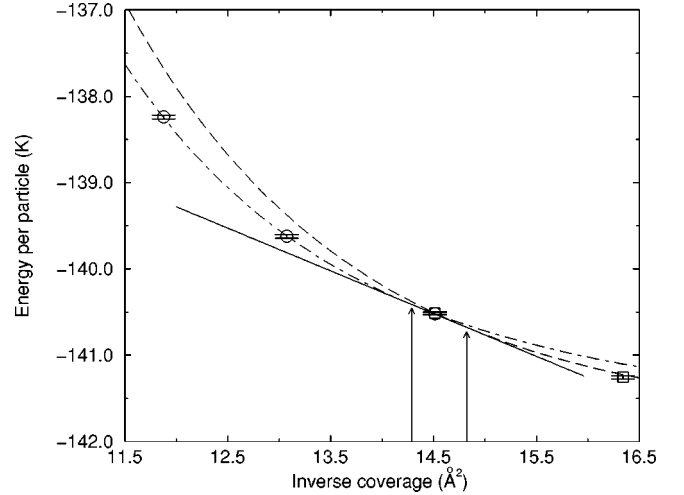


FIG. 3. Liquid-solid coexistence regions determined with the Maxwell construction. The dashed-dotted and dashed lines are the solid and liquid equations of state, respectively. Circles with error bars are calculated energy values for the liquid. Squares with error bars show values calculated for the solid phase. The unbroken line is the coexistence line. The arrows indicate the beginning and end of the coexistence region.

regions. The gas phase has zero density at zero temperature. We expect the liquid-gas phase to have two regions, one in which phase boundaries between these phases form, and one in which the liquid phase is artificially stretched. This is governed by the energy cost required to create the phase boundary. The metastable liquid phase is spatially indistinguishable from the equilibrium state, but the formation of droplets can be visualized. In Fig. 4 we plot the radial distribution function  $g(r)$  for the liquid at coverages in the droplet region, near equilibrium, and near the onset of liquid-solid coexistence. Here,  $r$  is the magnitude of the projection of the distance vector between two particles onto the plane of the substrate. In the droplet region, the long-range tail drops below unity, indicating the system does not uniformly cover the substrate. Near equilibrium the first peak has about the

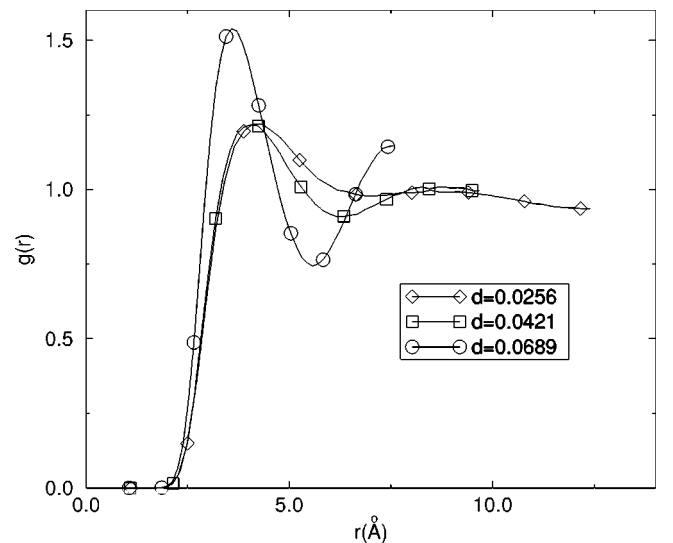


FIG. 4. Radial distribution function for the liquid phase at the indicated densities, in  $\text{atom}/\text{\AA}^2$ .

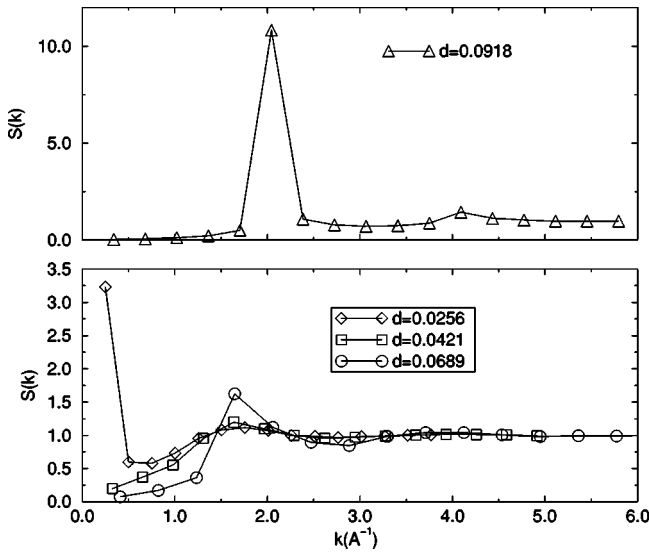


FIG. 5. Static structure function for the liquid phase at the indicated densities, in  $\text{atom}/\text{\AA}^2$ . The static structure function in the (01) direction at a typical solid density (top) is also shown.

same height as the droplet phase, but the tail goes to unity at long ranges. The peaks are located at the same value of  $r$ , indicating that the average separation distance of nearest-neighbor particles in the droplet is close to the equilibrium value. The peak height is 1.5, compared to 1.2 near equilibrium, and the peak's position has shifted from 4.2 to 3.6  $\text{\AA}$ , as one would expect from compression caused by increasing the density. These values are in agreement with values reported for the helium liquid in two dimensions,<sup>32</sup> indicating that the first-layer liquid is very two dimensional in character.

The results for the static structure factor  $S(k)$  for the liquid phase are shown in Fig. 5 and can be interpreted similarly. At the lowest coverage,  $S(k)$  swings upward for low values of  $k$  instead of going to zero. This indicates the presence of droplets and a nonzero compressibility. For the two uniform liquid coverages,  $S(k \rightarrow 0) \rightarrow 0$ . The structure function is more peaked for the high-density liquid. Figure 5 also shows results for a typical solid coverage. The peak heights for the fluid near equilibrium and for the dense fluid are 1.2 and 1.6, respectively. These values are in reasonable agreement with, but somewhat below, the two-dimensional values.

Finally, we show in Fig. 6 probability contours for the first layer for the various regions discussed above. The lowest coverage shown is below the spinodal point, and as expected incompletely covers the substrate. Near the equilibrium density, the substrate is uniformly covered. In the dense liquid, localization can be observed. This coverage is in the liquid-solid coexistence region. Finally the system enters a triangular solid phase at the highest density.

Promotion to the second layer may be determined by examining the density profiles for the dense solid. These are shown in Fig. 7 at the indicated coverages. The occupation of the second layer is clearly visible at the coverages 0.1200 and 0.1270  $\text{atom}/\text{\AA}^2$ , while the coverage 0.1180 shows no evidence of promotion. Integrating the profiles for the two largest coverages to the minimum between the peaks (4.5  $\text{\AA}$ ) gives 0.116 and 0.119  $\text{atom}/\text{\AA}^2$  for the first-layer coverage.

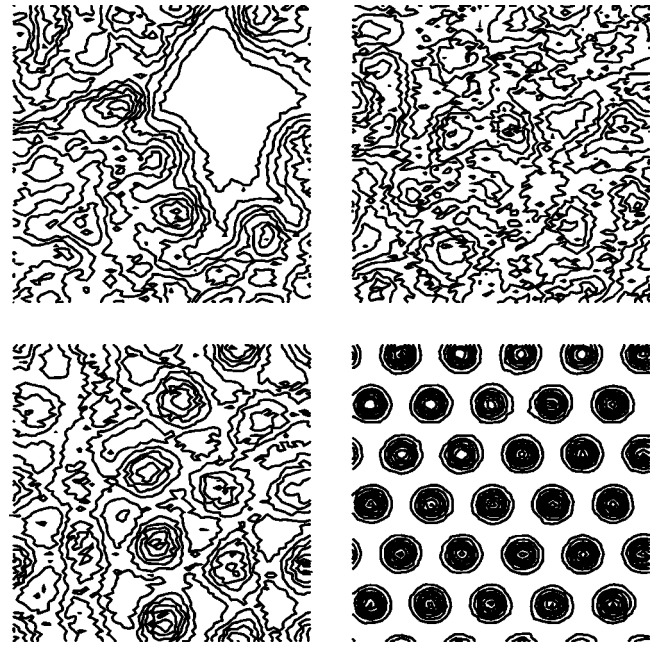


FIG. 6. Contour plots of the probability density in the plane of the substrate. The densities shown are, top row, left to right, 0.0256 and 0.0421  $\text{atom}/\text{\AA}^2$ ; bottom row, left to right, 0.0689 and 0.0918  $\text{atom}/\text{\AA}^2$ .

Experimentally, estimates<sup>15,36,37,5</sup> of first-layer completion range from 0.112 to 0.120  $\text{atom}/\text{\AA}^2$  so our value is in good agreement. The recent GFMC calculations<sup>24</sup> obtain a value between 0.115 and 0.118 for the beginning of the second-layer promotion.

#### IV. RESULTS WITH CORRUGATED SUBSTRATE

In this section we compare with the results obtained by using a more realistic model of the graphite substrate. Most of the results for the corrugated substrate were obtained with a simulation cell with the dimensions  $25.56 \times 22.14$   $\text{\AA}$ . The commensurate density corresponds to 36 helium atoms. Pe-

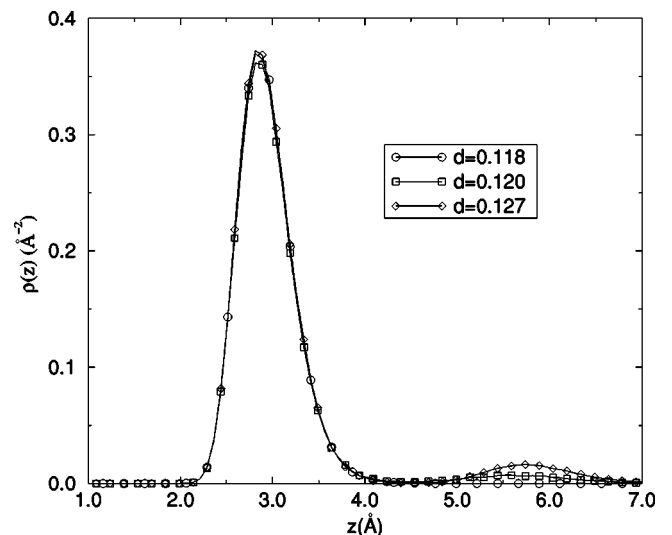


FIG. 7. Density profiles near the second-layer promotion. The coverages, in  $\text{atom}/\text{\AA}^2$ , are indicated. Normalization is chosen so that integrating the profiles gives the coverage.

riodic boundary conditions were used in the plane of the substrate. Finite-size effects were examined by repeating some calculations using a  $34.08 \times 29.51 \text{ \AA}$  simulation cell, for which the commensurate density corresponds to 64 particles.

### A. At and below commensurate density

The principal conclusion we obtain from these calculations is that the low-density, low-temperature phase of the first layer consists of commensurate solid clusters, rather than a liquid phase. In an earlier publication<sup>22</sup> we observed the commensurate phase and investigated its melting with both static structure and specific-heat calculations. The calculated  $\sqrt{3} \times \sqrt{3}$  commensurate solid phase and its melt were shown in Fig. 1 of Ref. 22. At 3 K, the film has solidified into the commensurate structure. The solid forms a sublattice that contains one-third of the adsorption sites. The remaining two-thirds of the sites form two equivalent sublattices that are unoccupied. Raising the temperature to 4 K causes melting. At this temperature the helium atoms no longer inhabit a single sublattice of substrate adsorption sites. All adsorption sites will be occupied with equal probability if the simulation is run for a sufficiently long time.

In Ref. 22 we presented evidence that the low-density (below the commensurate solid density of  $0.0634 \text{ atom/\AA}^2$ ) first layer consists of a solid cluster surrounded by a low-density vapor at low temperatures. No liquid phase forms and so there is no possibility for first-layer superfluidity. These findings are in contrast to the most recent proposal for this region.<sup>5</sup>

The presence of a solid with vacancies and phase separation was shown with contour plots of the probability distributions in Fig. 6 of Ref. 22. At lower temperature the vacancies condense into a single bubble region, while at higher temperature, the vacancies acquire enough kinetic energy to leave the phase-separated state and diffuse into the solid.

Figures 8 and 9 (not shown in our earlier paper) confirm that at density significantly lower than the commensurate density the system consists of solid clusters at low temperatures and that these clusters exhibit the melting behavior discussed in the preceding section. We have calculated distribution plots for densities as low as  $0.0207 \text{ atom/\AA}^2$  and observe solid clusters at all densities.

We have also attempted to place a vacancy in a solid cluster to see if the cluster could support an isolated vacancy and at the same time be in equilibrium with the low-density vapor. We found that at  $0.0424 \text{ atom/\AA}^2$  and 1.0 K, the vacancy was spontaneously expelled from the solid cluster during thermalization. We conclude that at low temperatures the solid clusters will not support isolated vacancies.

Further evidence for solidification into the commensurate structure in the simulation comes from calculations of the static structure factor. Typical results for static structure factors for coverages at and immediately below the commensurate solid density have been reported in our earlier paper.<sup>22</sup> The melting of the commensurate solid phase can be determined from the temperature dependence of the static structure peak height. Melting is signaled by a significant drop in the peak height and a large statistical fluctuation in a peak value near the melting temperatures. The melting tempera-

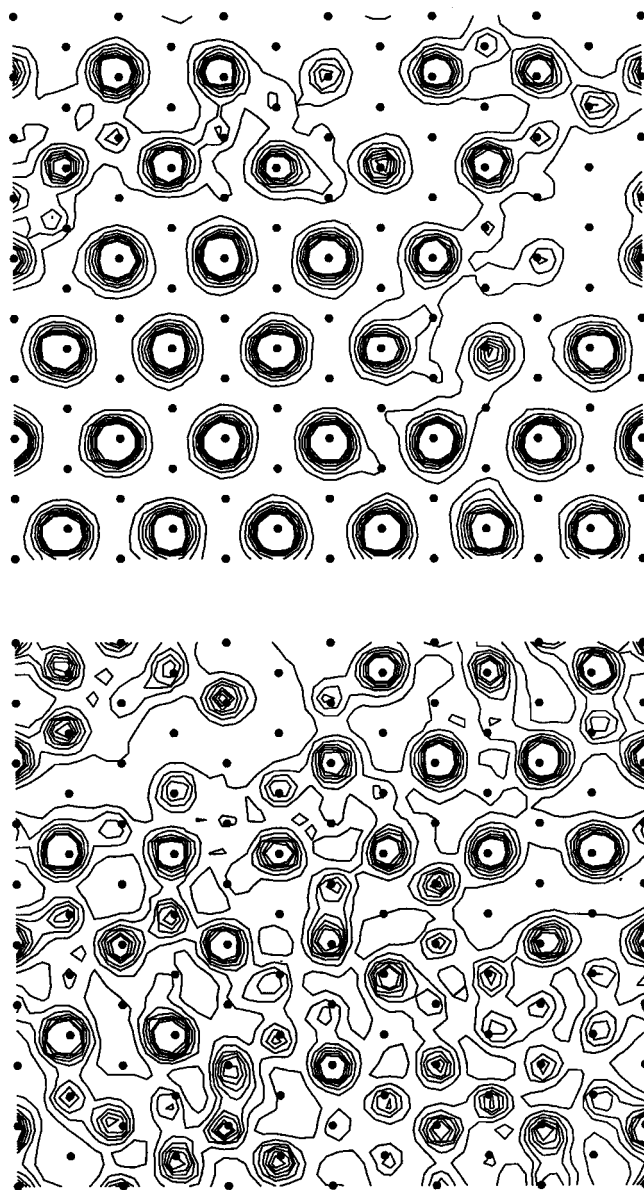


FIG. 8. Distribution plot at  $0.0530 \text{ atom/\AA}^2$ ,  $T = 2.5 \text{ K}$  (top), and  $T = 3.0 \text{ K}$  (bottom).

tures determined in this manner are given in Table II. The density dependence of the melting temperature is consistent with the experimental phase diagram, although our melting temperatures are slightly higher than the experimental values. Heat-capacity measurements indicate that the commensurate solid melts at about 3 K, and the low-density ( $< 0.045 \text{ atom/\AA}^2$ ) melting peaks are at about 1.5 K.

Another way of estimating melting temperatures is from the temperature dependence of the energy. This is shown in Fig. 10 for various densities. These curves possess inflection points that lead to specific-heat maxima when differentiated. These peaks indicate melting. Figure 4 or Ref. 22 shows two sample calculations of the specific heat at the indicated densities. The peak height and location change dramatically with density. Melting occurs at about 1.5 and 3.5 K for  $0.0353$  (circles) and  $0.0636 \text{ atom/\AA}^2$  (squares), respectively.

We have determined phase ranges by applying the Maxwell construction to the total ground-state energy. For a system at constant volume with a varying number of particles, a

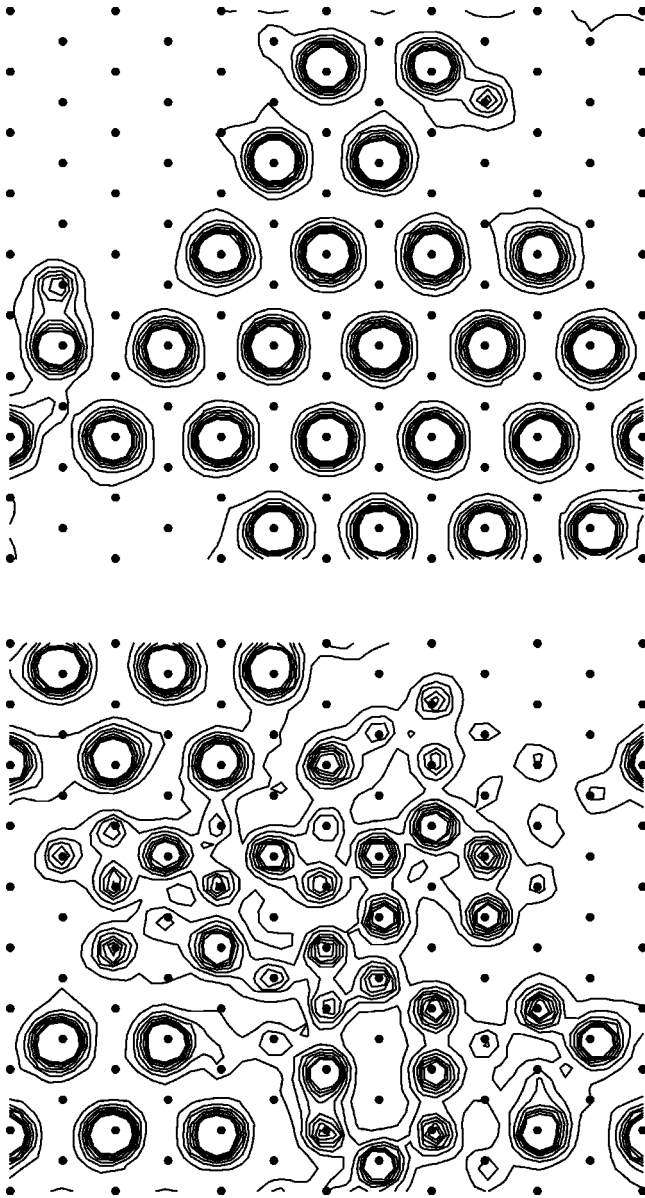


FIG. 9. Distribution plot at  $0.0424 \text{ atom}/\text{\AA}^2$ ,  $T=1.0 \text{ K}$  (top), and  $T=2.0 \text{ K}$  (bottom).

region of phase separation will be signaled by an unphysical upward curvature in the total free-energy's dependence on density. The upper and lower bounding densities of this region are connected by a common tangent line. The total free energy for all intermediate densities lies on or above this line, either because creating a surface between the two phases costs a finite amount of energy or because the system remains unphysically homogeneous. In the thermodynamic

TABLE II. Estimates of melting temperatures from the temperature dependence of the static structure peaks.

Coverage ( $\text{atom}/\text{\AA}^2$ )	$T_{melt}$
0.0424	2.0
0.0530	2.5
0.0566	3.0
0.0636	3.33

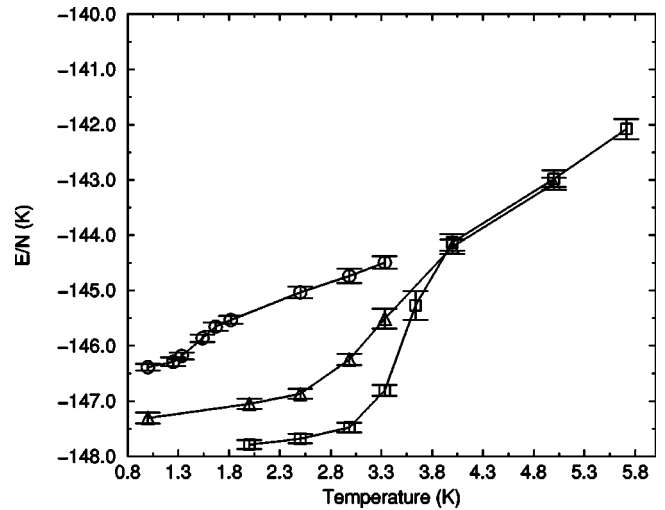


FIG. 10. Temperature dependence of the energy per particle. The coverages are  $0.0353$  (circles),  $0.0566$  (triangles), and  $0.0636 \text{ atom}/\text{\AA}^2$  (squares).

limit the system will separate into the two phases at the bounding densities.

The Maxwell construction at nonzero temperatures should be applied to the total free energy. This is not directly accessible from PIMC, however. Instead, we have used a limiting process to determine effectively ground-state energy values. All energy calculations were performed at low temperatures. The temperature is then raised and the energy is recalculated. If the two values are the same within error bars, we conclude that we have obtained effectively zero-temperature energy values. This allows us to apply the Maxwell construction to the total energy, since it is the same as the total free energy at zero temperature.

The values for the energy per particle for the first-layer solid are given in Table III for a range of densities including the commensurate density. The cell dimensions used here are  $25.560 \times 22.136 \text{ \AA}^2$ , and the number of particles varies from 20 to 40. Using these results we have applied the Maxwell construction in Fig. 5 of our previous publication.<sup>22</sup> Application of this method indicated that the intermediate energy values are unstable and will phase separate into the two stable phases (the vapor and the commensurate solid) that bound the unstable region.

Our result for the binding energy of a single particle on the substrate is  $E_B = -143.09 \pm 0.27$ . This value is comparable to the estimated values<sup>38</sup>  $E_B = -141.75 \pm 1.50 \text{ K}$  from

TABLE III. Energy per particle versus coverage. The first column gives the temperature of the calculation. The number in parentheses gives the error in the last decimal place.

T (K)	$\sigma(\text{\AA}^{-2})$	E/N (K)
1.00	0.0353	-143.73(8)
1.00	0.0424	-144.03(9)
1.00	0.0530	-144.31(7)
1.00	0.0566	-144.56(7)
1.00	0.0636	-145.12(8)
1.33	0.0707	-142.71(8)

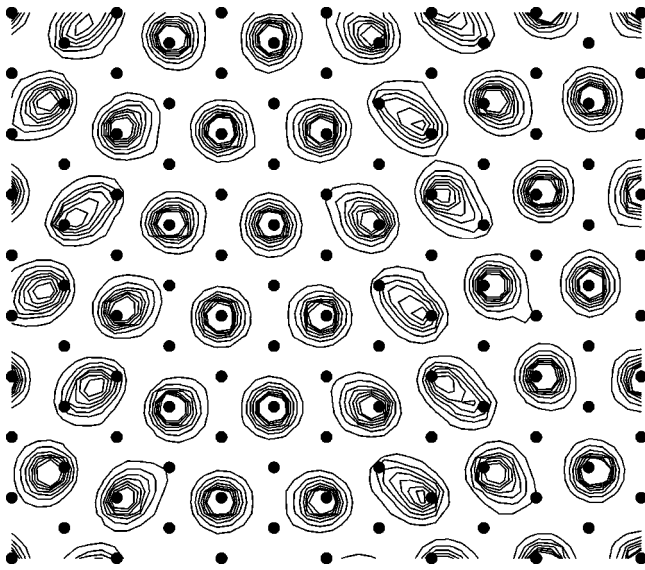


FIG. 11. Distribution plot of the domain-wall solid at  $0.0742 \text{ atom}/\text{\AA}^2$  ( $N=42$  atoms) and  $T=1.0$  K. Filled circles indicate adsorption sites.

scattering<sup>39,40</sup> and  $E_B = -142.33 \pm 1.97$  K from thermodynamic analysis.<sup>41</sup> Our value for the binding energy was calculated at 0.4 K and confirmed to be the ground-state value by the limiting procedure discussed above. By subtracting this energy from the energy per particle of the commensurate solid phase, we obtain the condensation energy per particle for the two-dimensional solid,  $E_{2D} = -2.03 \pm 0.20$  K. This is higher than the two-dimensional energy ( $-1.06$  K) for the commensurate phase found by the variational calculations of Ref. 20 for the same interaction model.

### B. Above commensurate density

We have simulated the first layer (with the inclusion of corrugations) at densities higher than the commensurate density up to the density where first-layer completion occurs. As a density is increasing, we find distinct phases: a domain-wall solid phase and an incommensurate solid phase at higher densities up to layer completion.

Figures 11 and 12 illustrate the domain-wall solid and incommensurate triangular solid phases, respectively. The domain-wall solid consists of patches of commensurate solid on different sublattices. Linear domain walls occur at the boundaries between these regions. In the incommensurate solid, the atoms form a triangular solid that does not have a periodic relationship with the underlying adsorption sites for length scales less than the minimum dimension of the simulation cell.

## V. TESTS OF OUR CONCLUSIONS

The applicability of our conclusions to the actual system may be limited by the accuracy of the interaction model that we use. First, it is possible that the substrate may substantially alter the helium-helium interaction.<sup>30,29</sup> Inclusion of this effect, the so-called McLachlan interaction, has been shown to change the ground-state phase from the commensurate solid to a low-density liquid in two-dimensional variational calculations.<sup>20</sup> We recalculated the low-temperature

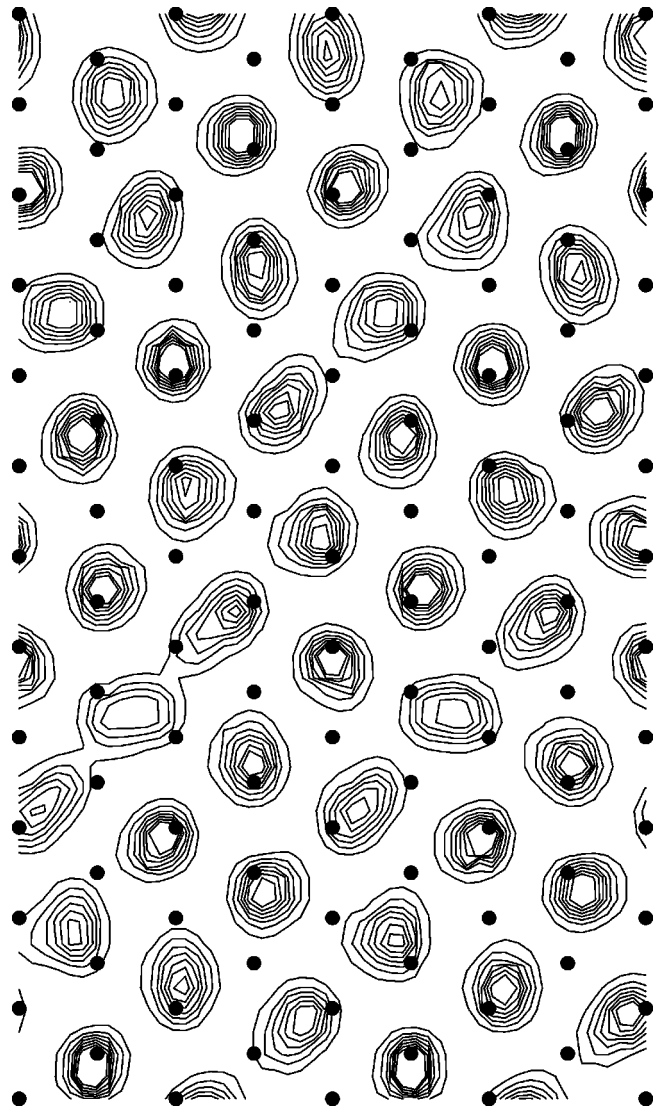


FIG. 12. Distribution plot of the incommensurate solid phase at  $0.0994 \text{ atom}/\text{\AA}^2$  ( $N=50$  atoms) and  $T=2.0$ . Filled circles indicate adsorption sites.

density scans using the same mediated interactions employed in these calculations.<sup>20</sup> We found that while the energy per particle increases for all coverages, the commensurate solid remains the energetically favored phase. Second, another possible problem might arise from a helium-graphite interaction<sup>23</sup> which could be too corrugated. We have calculated the total energy at low temperature, at the commensurate density, and at  $0.0424 \text{ atom}/\text{\AA}^2$  with the corrugation strength reduced by 25%. The commensurate phase remains energetically favored. Calculations were also performed with the corrugation reduced by 50%, but it was found that the commensurate solid would not form for temperatures as low as 2 K, thus indicating the corrugations had been underestimated. We note finally that the melting behavior of the commensurate solid phase was not sensitive to the inclusion of the McLachlan term.

The primary argument given by Greywalls and Busch against solid-vapor coexistence was that such coexistence should be signaled by linear heat-capacity isotherms for the entire region from zero coverage up to the commensurate density. We believe that the departure from linearity below

0.025 atom/Å<sup>2</sup> is caused by the presence of multiple finite-sized clusters. At low densities, solid clusters nucleate around surface defects. Initially, there are many small metastable clusters with large perimeter-to-area ratios. Increasing the density increases the size of the clusters until the surface is covered by a few large solid clusters with negligible boundary effects. Thus, the heat capacity exhibits linear behavior only after the solid clusters are sufficiently large so that the perimeter-to-area ratio is small. This presumably occurs for coverages above 0.025 atom/Å<sup>2</sup>.

In addition Greywall and Busch identified coverages near 0.04 atom/Å<sup>2</sup> as liquid. This conclusion was based partly on simulation results for 2D helium on a flat substrate, the most relevant calculations then available. As Greywall and Busch note, the large peak associated with the melting of the uniform commensurate solid phase first emerges above 0.04 atom/Å<sup>2</sup>. 2D helium is a liquid near this density,<sup>32</sup> suggesting that first-layer coverages below 0.04 may be liquid. Unlike the purely 2D simulations, our calculations take the role of substrate effects into account. In this paper we have explicitly studied both flat and corrugated substrate using a method which, given the interaction potentials, treats the problem exactly within statistical and finite-size errors. We have demonstrated that these errors are under control. We have shown that surface corrugations push the density corresponding to the energy minimum up from about 0.04 on a flat substrate to 0.0636 atom/Å<sup>2</sup> and produce solidification. Greywall and Busch also show that their low-density heat-capacity results are in general agreement with a PIMC calculation for 2D superfluid helium,<sup>42</sup> suggesting that there might be a superfluid transition in the first layer. However, as we have shown in Fig. 4 of our earlier publication<sup>22</sup> these rounded heat capacities are produced by the melting of a solid cluster and are not associated with a superfluid transition.

In closing, we would like to remark that a promising direction for monolayer superfluidity<sup>5,43-45</sup> lies with helium adsorbed on alkali-metal substrates, particularly lithium.<sup>46,44</sup> These substrates have much smaller corrugations and a much weaker attraction, allowing the first-layer helium film to be a liquid. The phenomenon competing with superfluidity for these substrates is pre-wetting, rather than solidification.

## VI. SUMMARY

Calculation for the first helium layer on graphite was performed both with and without substrate corrugations. When corrugations are neglected, the first-layer film resembles a purely two-dimensional film. We determined that the film consists of gas, liquid, and solid phases. These are separated by coexistence regions, and we determined the coverage ranges for all phases at low temperatures by using the Maxwell construction. The first-layer liquid has an equilibrium density of 0.0450 atoms/Å<sup>2</sup>. Below this density the system phase separates. This region is divided into an unstable region, where liquid droplets form, and a metastable region in which the system over-expands instead of forming an interface. These two regions are separated by a spinodal point at 0.034 atoms/Å<sup>2</sup>. At higher densities the system enters a narrow region of liquid-solid coexistence between 0.0675 and 0.0700 atoms/Å<sup>2</sup>. Above these coverages the system is in a triangular solid phase. The beginning of layer promotion occurs between 0.116 and 0.119 atoms/Å<sup>2</sup>. All of our calculations are in agreement with recent Green's-function Monte Carlo results.<sup>24</sup>

When corrugations are included in the first layer, the phase diagram is substantially altered. We find that a  $\sqrt{3} \times \sqrt{3}$  commensurate solid occurs, in agreement with numerous experiments. By examining the temperature dependence of the static structure function and the specific heat, we find that this solid melts at approximately 3.5 K, compared with the experimental melting temperature of 3 K. We further find that the commensurate solid phase is energetically favored. At densities below commensuration, the system phase separates into commensurate solid clusters and a low-density vapor. No liquid phase occurs at low temperatures.

## ACKNOWLEDGMENTS

This work was supported in part by the National Aeronautics and Space Administration under Grant No. NAG3-1841. Some of the calculations were performed using the facilities of the Supercomputer Computations Research Institute at Florida State University. We also wish to thank L. W. Bruch for useful comments on our work.

<sup>1</sup>J. G. Dash, *Films on Solid Surfaces* (Academic, New York, 1975).

<sup>2</sup>M. Schick, in *Phase Transitions in Surface Films*, edited by J. G. Dash and J. Ruvalds (Plenum, New York, 1980).

<sup>3</sup>L. W. Bruch, M. W. Cole, and E. Zaremba, *Physical Adsorption: Forces and Phenomena* (Oxford, New York, 1997).

<sup>4</sup>M. Bretz, Phys. Rev. Lett. **38**, 501 (1977).

<sup>5</sup>D. S. Greywall and P. A. Busch, Phys. Rev. Lett. **67**, 3535 (1991).

<sup>6</sup>D. S. Greywall, Phys. Rev. B **47**, 309 (1993).

<sup>7</sup>P. A. Crowell and J. D. Reppy, Physica B **187**, 278 (1994).

<sup>8</sup>P. A. Crowell and J. D. Reppy, Phys. Rev. B **53**, 2701 (1996).

<sup>9</sup>M. Nielsen, J. P. McTague, and L. Passell, in *Phase Transitions in Surface Films*, edited by J. G. Dash and J. Ruvalds (Plenum, New York, 1980).

<sup>10</sup>F. F. Abraham and J. Q. Broughton, Phys. Rev. Lett. **59**, 64 (1987).

<sup>11</sup>K. Carneiro *et al.*, Phys. Rev. Lett. **37**, 1695 (1976).

<sup>12</sup>S. V. Hering, S. W. V. Sciver, and O. E. Vilches, J. Low Temp. Phys. **25**, 793 (1976).

<sup>13</sup>T. A. Rabedeau, Phys. Rev. B **39**, 9643 (1989).

<sup>14</sup>R. E. Ecke, Q.-S. Shu, T. S. Sullivan, and O. E. Vilches, Phys. Rev. B **31**, 448 (1985).

<sup>15</sup>M. Bretz, Phys. Rev. Lett. **31**, 1447 (1973).

<sup>16</sup>A. N. Berker, S. Ostlund, and F. A. Putnam, Phys. Rev. B **17**, 3650 (1978).

<sup>17</sup>M. Schick, J. S. Walker, and M. Wortis, Phys. Rev. B **16**, 2205 (1977).

<sup>18</sup>M. J. Tejwani, O. Ferreira, and O. E. Vilches, Phys. Rev. Lett. **44**, 152 (1980).

- <sup>19</sup>S. B. Crary and D. A. Fahey, *Phys. Rev. B* **35**, 2102 (1987).
- <sup>20</sup>J. M. Gottlieb and L. W. Bruch, *Phys. Rev. B* **48**, 3943 (1993).
- <sup>21</sup>P. Mohandas *et al.*, *J. Low Temp. Phys.* **101**, 481 (1995).
- <sup>22</sup>M. Pierce and E. Manousakis, *Phys. Rev. Lett.* **83**, 5314 (1999).
- <sup>23</sup>W. E. Carlos and M. W. Cole, *Surf. Sci.* **91**, 339 (1980).
- <sup>24</sup>P. A. Whitlock, G. V. Chester, and B. Krishnamachari, *Phys. Rev. B* **58**, 8704 (1998).
- <sup>25</sup>D. M. Ceperley, *Rev. Mod. Phys.* **67**, 279 (1995).
- <sup>26</sup>M. Pierce and E. Manousakis, *Phys. Rev. B* **59**, 3802 (1999).
- <sup>27</sup>M. Takahashi and M. Imada, *J. Phys. Soc. Jpn.* **53**, 3765 (1984).
- <sup>28</sup>R. A. Aziz *et al.*, *Mol. Phys.* **77**, 321 (1992).
- <sup>29</sup>L. W. Bruch, *Surf. Sci.* **125**, 194 (1982).
- <sup>30</sup>A. D. McLachlan, *Mol. Phys.* **7**, 381 (1964).
- <sup>31</sup>R. A. Aziz *et al.*, *J. Chem. Phys.* **70**, 4330 (1979).
- <sup>32</sup>P. A. Whitlock, G. V. Chester, and M. H. Kalos, *Phys. Rev. B* **38**, 2418 (1988).
- <sup>33</sup>S. Giorgini, J. Boronat, and J. Casulleras, *Phys. Rev. B* **54**, 6099 (1996).
- <sup>34</sup>B. E. Clements, J. L. Epstein, E. Krotcheck, and M. Saarela, *Phys. Rev. B* **48**, 7450 (1993).
- <sup>35</sup>M. C. Gordillo and D. M. Ceperley, *Phys. Rev. B* **58**, 6447 (1998).
- <sup>36</sup>S. E. Polanco and M. Bretz, *Phys. Rev. B* **17**, 151 (1978).
- <sup>37</sup>K. Carneiro, L. Passell, W. Thomlinson, and H. Taub, *Phys. Rev. B* **24**, 1170 (1981).
- <sup>38</sup>M. W. Cole and D. L. Goodstein, *Rev. Mod. Phys.* **53**, 199 (1981).
- <sup>39</sup>G. D. Derry, D. Wesner, W. E. Carlos, and D. R. Frankl, *Surf. Sci.* **87**, 629 (1979).
- <sup>40</sup>W. E. Carlos and M. W. Cole, *Phys. Rev. B* **21**, 3713 (1980).
- <sup>41</sup>R. L. Elgin and L. Goodstein, *Phys. Rev. A* **9**, 2657 (1974).
- <sup>42</sup>D. M. Ceperley and E. L. Pollock, *Phys. Rev. B* **39**, 2084 (1989).
- <sup>43</sup>J. M. Mochel and M.-T. Chen, *Phys. Rev. B* **197**, 278 (1994).
- <sup>44</sup>M. Boninsegni and M. W. Cole, *J. Low Temp. Phys.* **113**, 393 (1998).
- <sup>45</sup>J. Nyéki, R. Ray, B. Cowan, and J. Saunders, *Phys. Rev. Lett.* **81**, 152 (1998).
- <sup>46</sup>E. Cheng, G. Ihm, and M. W. Cole, *J. Low Temp. Phys.* **74**, 519 (1989).